

## Supplementary Materials for

### **Gamma rhythm communication between entorhinal cortex and dentate gyrus neuronal assemblies**

Antonio Fernández-Ruiz\*, Azahara Oliva, Marisol Soula, Florbela Rocha-Almeida,  
Gergo A. Nagy, Gonzalo Martín-Vazquez, György Buzsáki\*

\*Corresponding author. Email: gyorgy.buzsaki@nyumc.org (G.B.); afr77@cornell.edu (A.F.-R.)

Published 2 March 2021, *Science* **372**, eabf3119 (2021)  
DOI: 10.1126/science.abf3119

#### This PDF file includes:

Figs. S1 to S14

**Other Supplementary Material for this manuscript includes the following:**  
(available at [science.scienmag.org/content/372/6537/eabf3119/suppl/DC1](https://science.scienmag.org/content/372/6537/eabf3119/suppl/DC1))

MDAR Reproducibility Checklist (PDF)

## Supplemental Figures

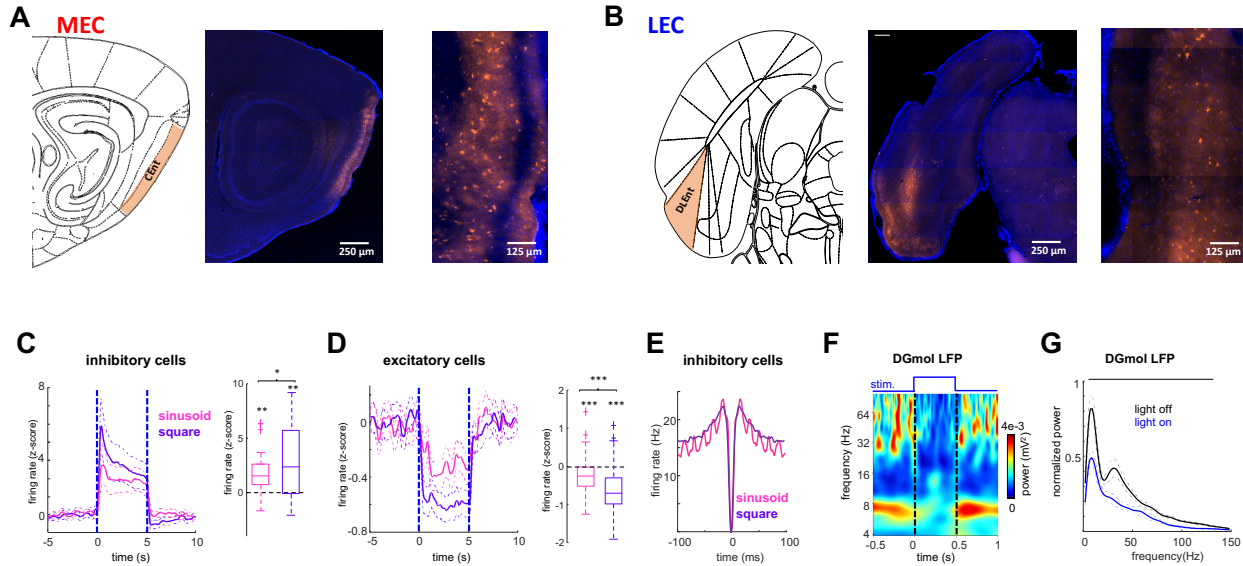


**Figure S1: Effect of optogenetic perturbation on the firing of entorhinal units**

**A)** Sagittal histological sections showing the expression of AAV5-mDlx-ChR2-mCherry (orange) in GABAergic cells in the MEC of a representative animal. Blue is DAPI staining. **B)** Coronal histological sections showing the expression of AAV5-mDlx-ChR2-mCherry (orange) in GABAergic cells in the LEC of a different rat. **C-J)** Entorhinal local perturbation and recording experiment ( $n= 2$  rats). Entorhinal cells were recorded 3 weeks after AAV5-mDlx-ChR2-mCherry local injection with a silicon probe glued to a 200- $\mu$ m optic fiber for blue light delivery. **C)** Responses of MEC putative inhibitory ( $n = 16$  units) and **(D)** excitatory ( $n = 86$ ) entorhinal cortical cells to 5s of 53 Hz blue light (450 nm) sinusoidal stimulation or continuous light stimulation of the same intensity (mean  $\pm$  SEM). Dashed blue lines indicate stimulation onset and offset. Boxplot: quantification of average firing response across all inhibitory and excitatory cells showing a significant increase and decrease, respectively (\*\*/\*\*\*  $P < 0.01/0.001$ , sign-rank test). Note that continuous light stimulation exerted a stronger and faster-accommodating effect on firing rates than sinusoidal stimulation (\*/\*\*  $P < 0.05/0.001$ , rank-sum test). **E)** Average autocorrelograms of inhibitory cells during light on periods show rhythmic entrainment to 53 Hz stimulation. **F)** Example wavelet spectrogram of DG molecular layer LFP during a 500 ms MEC continuous light stimulation to illustrate the strong suppression of both theta and gamma oscillations in the hippocampus. **G)** Average power spectrum of DG molecular layer LFP during epochs of MEC continuous light on and off (5s trials; only epochs with movement,  $>5$  cm/s, were included) show strong wide-band power reduction (continuous line: difference light off / light on,  $P < 0.05$ , with Bonferroni correction).

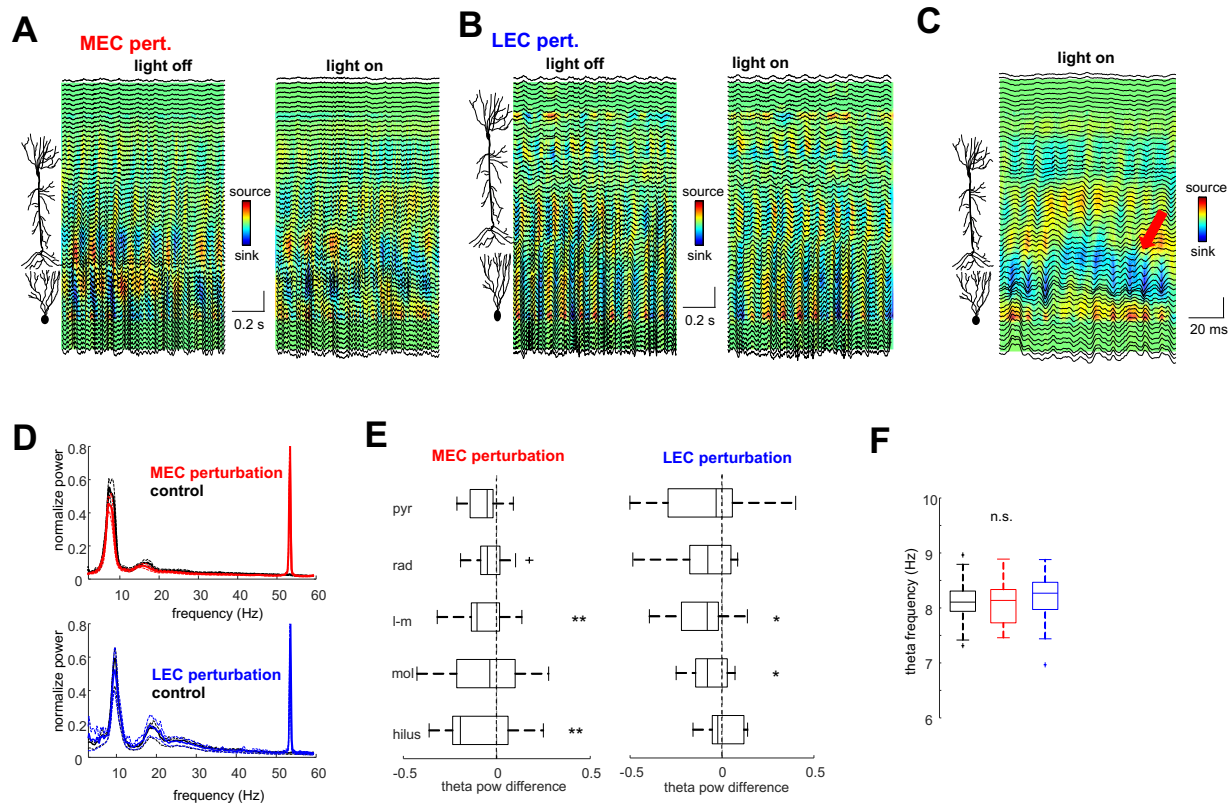


**Figure S2: Effect of optogenetic perturbation on hippocampal theta oscillations**

**A)** LFP and CSD depth profiles, recorded with a linear electrode implanted in the hippocampus (64 channels, 20  $\mu$ m spaced), from a representative animal with MEC perturbation. One seconds of light-off (left) and a light-on (right) epochs are shown. Neurons on the left indicate the relative position of CA1 and DG layers. **B)** Same layout as in A) but from a different animal with ChR2 expression in the LEC. **C)** Short epoch (200 ms) illustrating the presence of artificial gamma oscillation (arrow) in the str. lacunosum-moleculare of CA1 and in the DG molecular layer during MEC optogenetic perturbation. Vertical scale bars in A-C are 0.5 mV. **D)** Average power spectrums for LFP recorded in the hippocampal fissure during learning trials normalized to baseline power. Upper plot show data from 6 rats during control and MEC perturbation sessions and lower plots from another 6 animals during control and LEC perturbation sessions. Note the moderate reduction of theta power during both MEC and LEC perturbations and the presence of a peak corresponding to the stimulation frequency (53 Hz). Note also that optogenetic perturbation did not entrain the native gamma oscillation but, rather, added a narrow artificial band with spikes entrained to this band (Fig. 1F, G and Fig. S1E). **E)** Theta (5-15 Hz) power difference [(baseline-perturb.)/(baseline+perturb.)] for MEC and LEC perturbation sessions ( $n = 14/14$  sessions from 6 animals in each case) calculated for LFPs recorded in different hippocampal layers. \*/\*\*  $P < 0.01/0.001$ , sign-rank test. pyr = CA1 pyramidal layer, rad= stratum radiatum, l-m= stratum lacunosum-moleculare, mol= molecular layer, hil= hilus. **F)** Mean theta frequency during control, MEC perturbation and LEC perturbation learning trials for the spatial, object and object-in place tasks were not significantly different ( $F_{(2,38)} = 2.5$ ,  $P > 0.05$ , one-way ANOVA)). Only epochs with speed above 5 cm/s were included in these analyses.

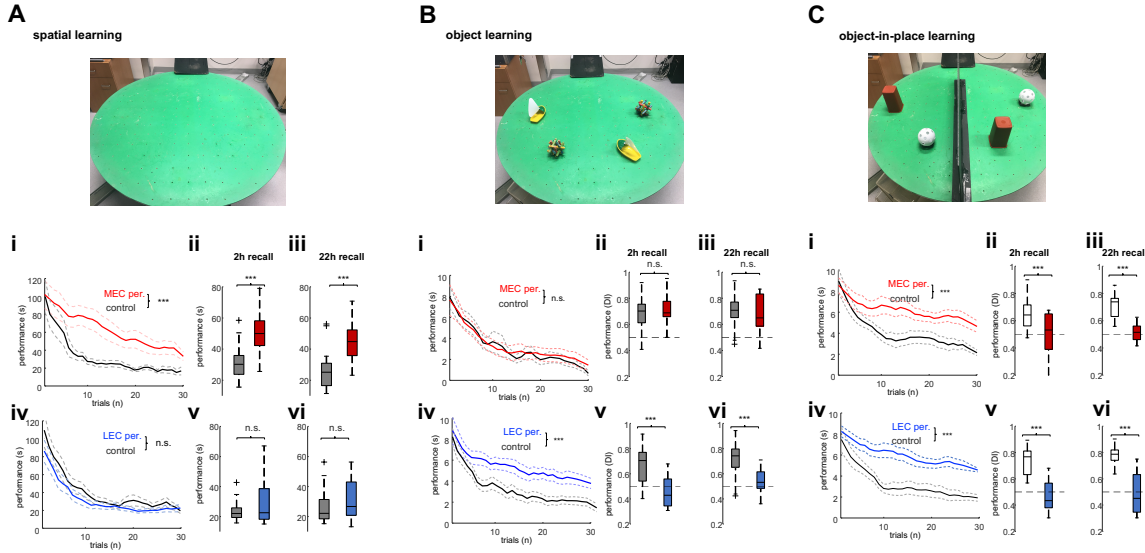


**Figure S3: Learning performance in the cheeseboard maze tasks**

**A)** Top: Photograph of the cheeseboard maze set up for the spatial learning task. Water rewards were placed in three different wells of the 177 that tiled the floor of the maze on each day. Bottom: Behavioral performance data from each of the two cohorts of 6 rats (one for MEC and the other for LEC perturbation) that were pooled together in Fig. 1. **i** - Learning performance quantified as time spent to find the 3 rewards on the maze during control and MEC perturbation sessions. ANOVA with repeated measures showed a significant main effect of group ( $F_{(1,33)} = 90.1$ ,  $P < 10^{-10}$ ). \*\*\*  $P < 0.0001$ , Tukey's post-hoc test. **ii** - Memory performance during recall test 2 hours ( $P = 3.8\text{e-}4$ , rank-sum test) or 22 (iii) hours after learning ( $P = 5.4\text{e-}4$ ). **iv** - LEC perturbation did not affect learning performance ( $F_{(1,25)} = 2.7$ ,  $P > 0.05$ , ANOVA) or recall 2h (v -  $P > 0.05$ , rank-sum test) or 22h later (vi -  $P > 0.05$ ). **B)** Top: picture of the cheeseboard maze set up for the object learning task. In this case, reward was hidden in two wells around each of the plastic boats while the wooden sticks objects acted as distractors. Bottom: behavioral performance for the MEC and LEC perturbation cohorts. **i** - Learning performance was quantified as time spent exploring around distractor objects during trials and not affected by MEC perturbation ( $F_{(1,27)} = 0.03$ ,  $P > 0.05$ , ANOVA). Performance during probes was measured with a discrimination index. Rats correctly remember the previously baited objects 2h (ii -  $P = 1.9\text{e-}6$ /  $4.4\text{e-}4$  for control and MEC perturbation sessions, sign-rank test. No difference between control and MEC perturbation sessions,  $P > 0.05$ , rank-sum test) and 22h after learning 2h (iii -  $P = 2.6\text{e-}6$ /  $7.1\text{e-}4$  sign-rank test. No difference between control and MEC perturbation sessions,  $P > 0.05$ , rank-sum test). **iv** - LEC perturbation reduced learning performance ( $F_{(1,28)} = 98.2$ ,  $P < 10^{-22}$ , ANOVA) and recall 2h (v -,  $P > 2.3\text{e-}5$ , rank-sum test) or 22h later (vi -  $P > 9.8\text{e-}4$ ). **C)** Object-in-place learning task. Same layout as in B. In the example depicted in the picture, the red block was baited in the left side of the maze and it served as a distractor on the right side, while for the white perforated ball it was the opposite. Learning performance was quantified as in the object learning task ( $n = 4/4$  rats in MEC and LEC cohorts). **i** - Learning performance was reduced by MEC perturbation ( $F_{(1,21)} = 85.8$ ,  $P < 10^{-10}$ , ANOVA). Correct recall of the baited objects was impaired 2h (ii -  $P = 0.03$  for control versus MEC perturbation sessions, rank-sum test) and 22h after learning 2h (iii -  $P = 3.2\text{e-}4$ ). **iv** - LEC perturbation also reduced learning performance ( $F_{(1,21)} = 188.7$ ,  $P < 10^{-10}$ , ANOVA) and recall 2h (v -  $P = 1.6\text{e-}3$ , rank-sum test) or 22h later (vi -  $P = 3.7\text{e-}4$ ).

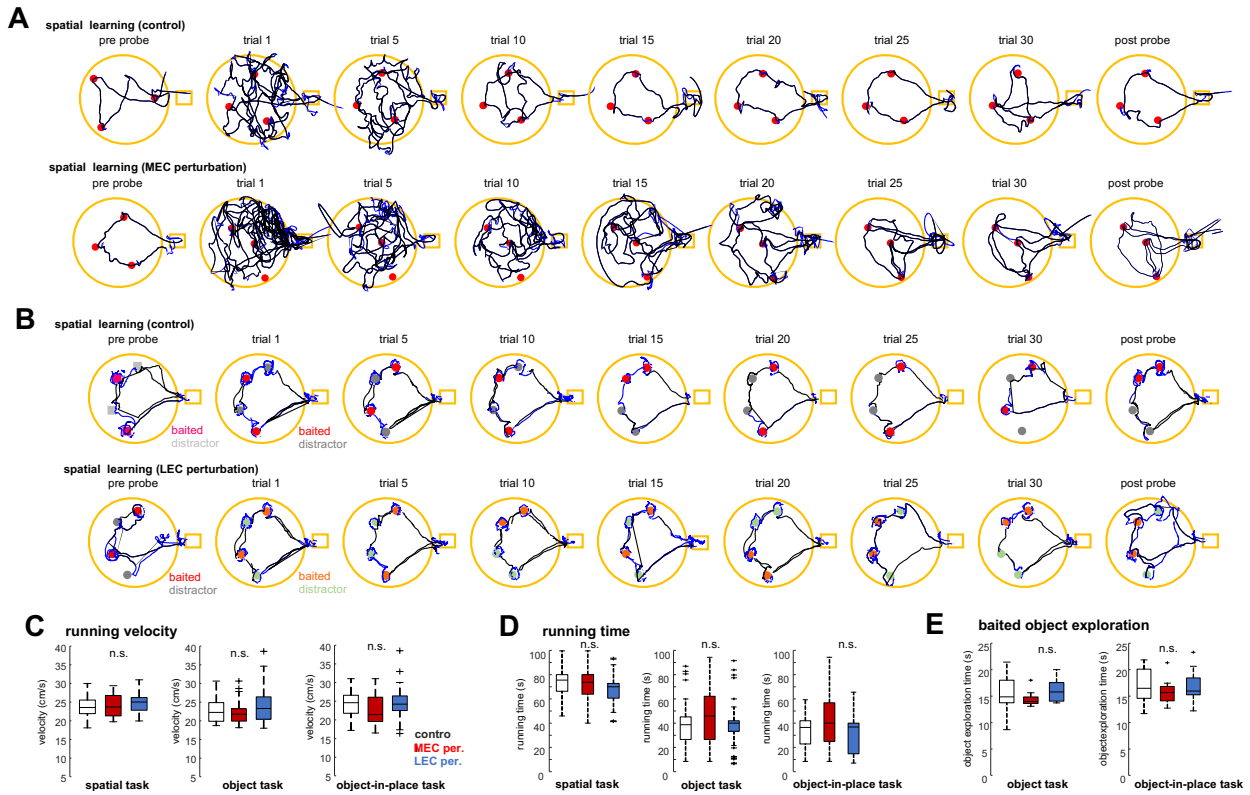


**Figure S4: Exploratory behavior in the cheeseboard maze tasks**

**A)** Example of exploration trajectories during pre-probe (with previous day reward configuration) and 2h post-learning test probe and successive learning trials in the spatial learning task for one control session (first row) and next day MEC perturbation session (below). Each plot is one trial. Black lines are animal's path when running speed was above 5 cm/s and blue lines when it was below. Red circles denote reward locations. **B)** Same layout as in A but for the object learning task for another animal with LEC ChR2 expression. Each plot is one trial or the first 3 min for probe sessions. **C)** Average running velocity (only periods with speed above 5 cm/s were included) during control, MEC perturbation and LEC perturbation learning trials for the spatial ( $F_{(2,60)} = 1.1$ ,  $P > 0.05$ , one-way ANOVA), object ( $F_{(2,57)} = 2.6$ ,  $P > 0.05$ , one-way ANOVA) and object-in-place tasks ( $F_{(2,44)} = 2.8$ ,  $P > 0.05$ , one-way ANOVA). **D)** Fraction of trial time spent running above 5 cm/s during control, MEC perturbation and LEC perturbation learning trials for the spatial ( $F_{(2,60)} = 2.2$ ,  $P > 0.05$ , one-way ANOVA), object ( $F_{(2,57)} = 1.7$ ,  $P > 0.05$ , one-way ANOVA) and object-in place tasks ( $F_{(2,44)} = 2.9$ ,  $P > 0.05$ , one-way ANOVA). **E)** Time spent exploring the baited objects during control, MEC perturbation and LEC perturbation learning trials for the object ( $F_{(2,57)} = 0.98$ ,  $P > 0.05$ , one-way ANOVA) and object-in place tasks ( $F_{(2,44)} = 0.3$ ,  $P > 0.05$ , one-way ANOVA).

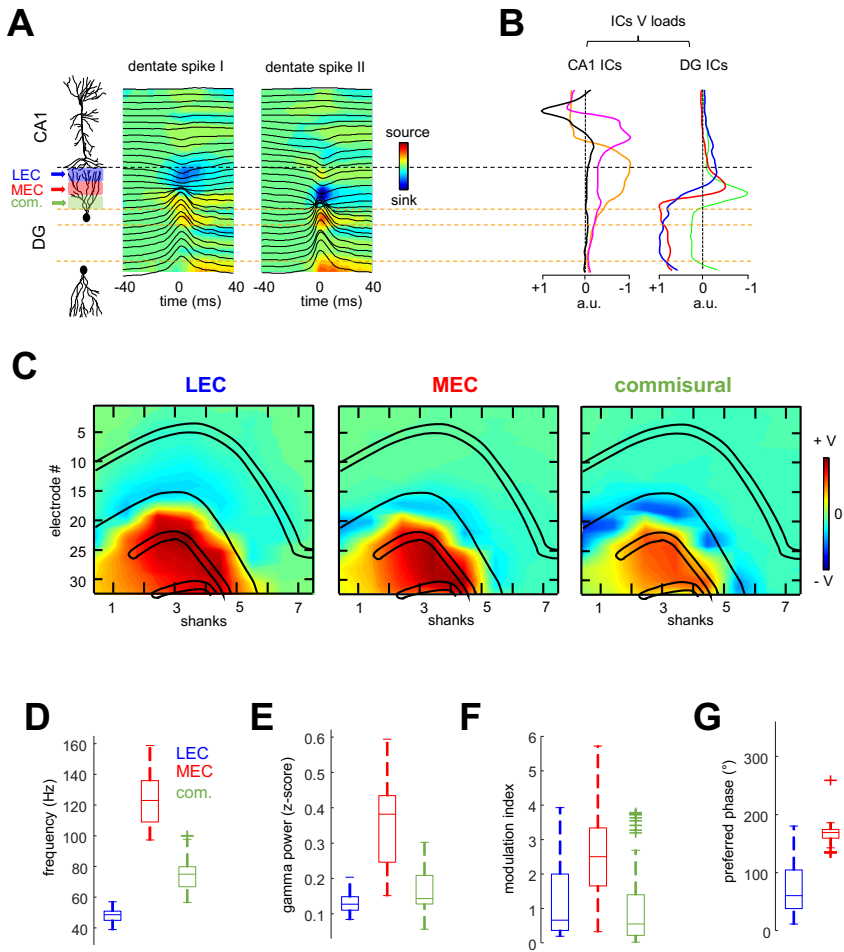


**Figure S5: Characterization of MEC and LEC gamma oscillations in the DG-CA3 regions**

**A)** Depth profiles of type I and type II LFP dentate spikes show current sinks in the outer and middle molecular layer, the synaptic domains of lateral (LEC) and medial (MEC) performant pathways respectively. LFPs correspond to a single vertical shank (32 recording sites spaced 50  $\mu\text{m}$ ). **B)** ICA decomposition of LFPs from the same shank result in 6 main components, 3 with currents restricted to the CA1 area (left plot) and 3 with currents in the DG (right plot). Each color line corresponds to one IC's depth voltage profile. The three DG ICs were classified according the location of maximal negative voltage and current sink amplitude. LEC IC (blue) peaked in the outer molecular layer, MEC IC (red) in the middle and commissural IC (green) in the innermost third of the molecular layer. They also showed a polarity reversal (from negative to positive) at different depths in the molecular layer. **C)** Two-dimensional voltage maps of DG ICs were back-projected to the anatomical recoding space (8 shanks spaced 300  $\mu\text{m}$  with 32 recording sites each shank). The electrode array was placed parallel to the transverse axis of the dorsal hippocampus spanning from CA1 pyramidal layer to lower blade of DG. Compare these panels with the 2-D CSD maps shown in Fig. 3D. **D-G)** Spectral characteristics of LEC, MEC and commissural ICs ( $n = 12$  animals): peak frequency (**D**), mean gamma power (**E**), gamma amplitude-theta phase modulation index (**F**) and preferred theta phase of spiking (**G**).

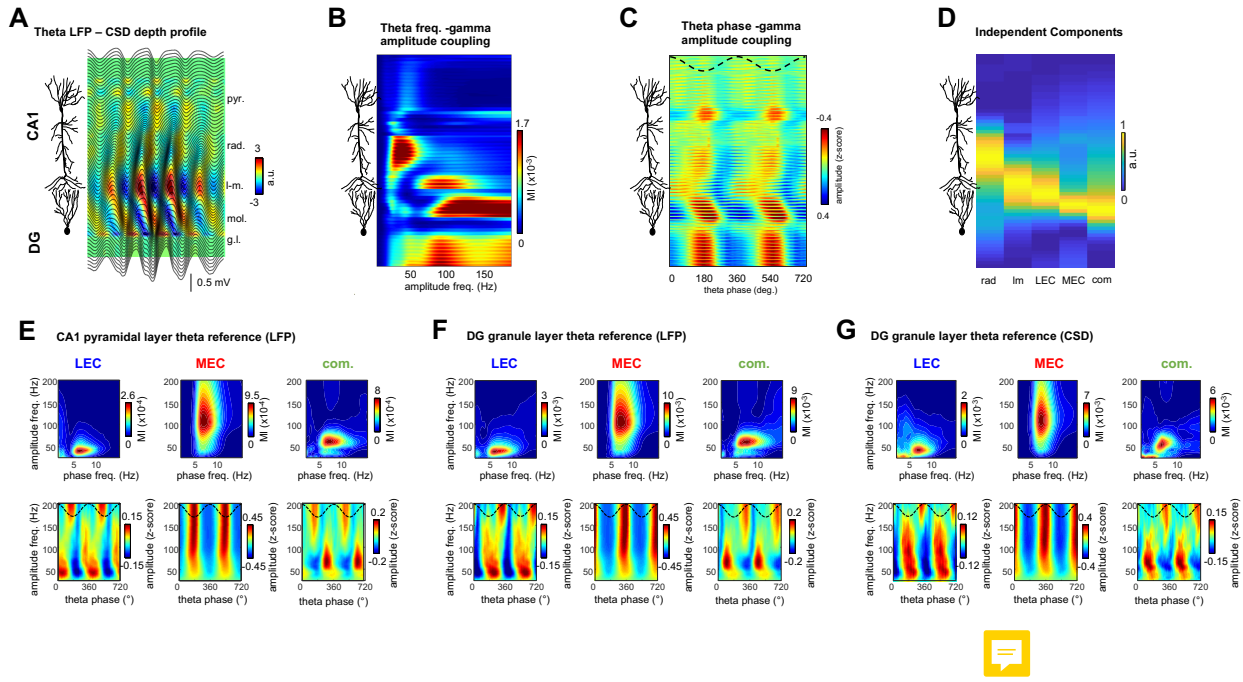


**Figure S6: Theta-gamma cross-frequency coupling in the DG**

**A-D)** Example laminar LFP profile recoded with a 64-site linear probe (20  $\mu\text{m}$  inter-site distance) across CA1 and DG layers (A and B were reproduced from Figure 3). **A)** Depth profile of averaged theta LFPs superimposed on CSD map. pyr = CA1 pyramidal layer, rad= stratum radiatum, l-m = stratum lacunosum-moleculare, mol = molecular layer, gl = granule cell layer, DG, dentate gyrus. **B)** Gamma amplitude - theta frequency comodulograms for each recording site (LFP) were concatenated into a single matrix. **C)** Gamma amplitude - theta phase (CA1 pyr layer) comodulograms were concatenated in a single matrix in the same way as in **B**. **D)** ICA decomposition of LFPs along the CA1-DG axis resulted in two main independent components (ICs) in CA1 (radiatum [rad] and lacunosum-moleculare [lm] ICs) and three in the DG (LEC, MEC and commissural [com]). Each line of the matrix represents the spatial weights of one IC. **E-G)** Gamma amplitude - theta frequency (upper row) and gamma amplitude - theta phase comodulograms (bottom row) for the 3 DG ICs extracted from the same recording as in A-D but now related to different reference theta signals: CA1 pyramidal layer LFP (**E**), DG granule layer LFP (**F**) and DG granule layer CSD (**G**). Note that the same gamma sub-bands were identified in each case (gammas, gammam and gammaf) but their theta phase preference was shifted  $\sim 180^\circ$  when using DG LFP or CSD compared to CA1 pyramidal layer reference.

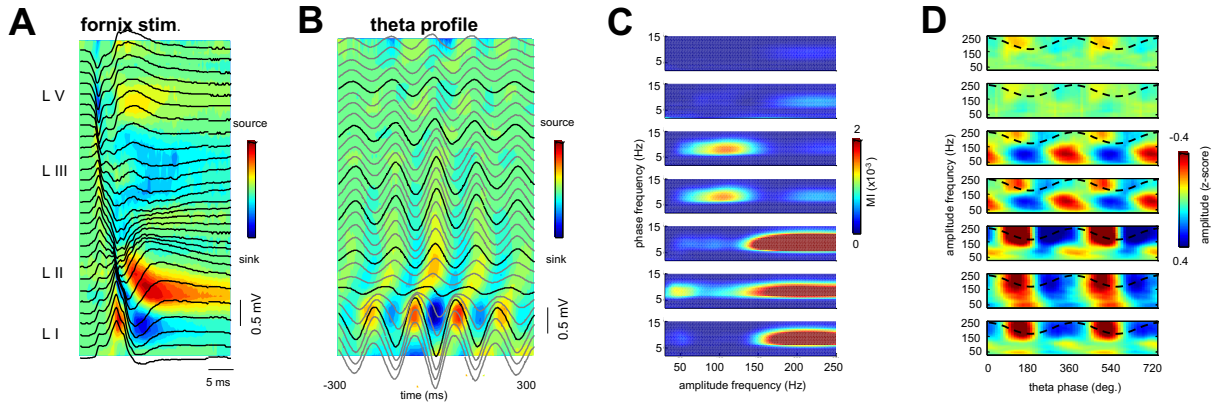


**Figure S7: Laminar and spectral properties of entorhinal oscillations**

**A)** LFP and CSD (colormaps) depth profile from a single-shank linear probe inserted approximately perpendicular to dorsal MEC cellular layers on an example session, showing evoked response to ipsilateral fornix stimulation. Electrical stimulation elicited a short latency population spike in layer V and a larger latency one in layer II, both followed by slower suppression of responses. **B)** Averaged theta LFPs and CSD showing characteristic phase shift of theta oscillations that reversed in polarity between layer 2 and layer 1. **C)** Gamma amplitude-theta frequency comodulograms for each recording site highlighted in **A**, illustrating the presence of several layer-specific gamma oscillations. **D)** Gamma amplitude-theta phase comodulograms for the same recording sites as in **A**. Theta reference was taken from the CA1 pyramidal layer. Note that layer III LFP traces were dominated by  $\gamma_M$  oscillations at the CA1 theta peak while layer II by  $\gamma_F$  oscillations at the theta trough.

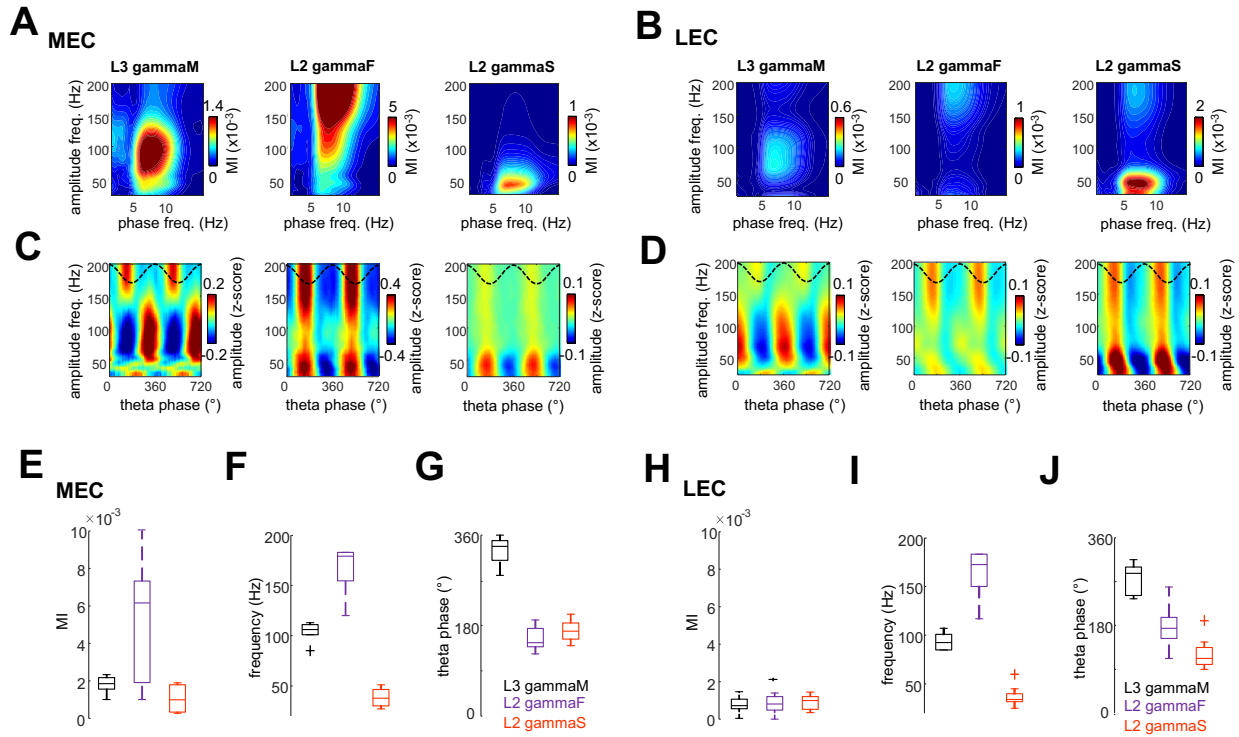


**Figure S8: Spectral properties of layer-specific gamma oscillations in MEC and LEC**

ICA decomposition of MEC and LEC LFPs identified three main sources of gamma oscillations: a mid-frequency gamma rhythm in layer III (60-100 Hz,  $\text{gamma}_M$ ), fast frequency gamma in layer II (120-200 Hz,  $\text{gamma}_F$ ) and slow-frequency gamma also in layer II (30-50 Hz,  $\text{gamma}_S$ ). **A)** Gamma amplitude-theta frequency (GA-TF) comodulograms for each MEC (**A**) and LEC (**B**) ICs displayed modulation in a specific gamma sub-band (group data from  $n = 4$  rats for MEC and 4 for LEC). Note that while each gamma sub-bands are present in both MEC and LEC, the strength of the L3  $\text{gamma}_M$  and L2  $\text{gamma}_F$  is considerably higher in MEC than in LEC, and the opposite is the case for L2  $\text{gamma}_S$ . The different MEC (**C**) and LEC (**D**) layer-specific gamma components occur at different phases of the reference theta (CA1 pyramidal layer) cycle: L3  $\text{gamma}_M$  at the theta peak and L2  $\text{gamma}_F$  and  $\text{gamma}_S$  near to the trough, coinciding with the preferred firing phase of entorhinal L3 and L2 principal units, respectively<sup>47</sup>. **E-J)** Spectral characteristics of MEC and LEC ICs ( $n = 12/12$  sessions from 4 MEC and 4 LEC animals): GA-TF modulation index for MEC (**E**) and LEC (**H**); peak gamma frequency for MEC (**F**) and LEC (**I**); preferred theta phase of sub-gamma bands for MEC (**G**) and LEC (**J**).

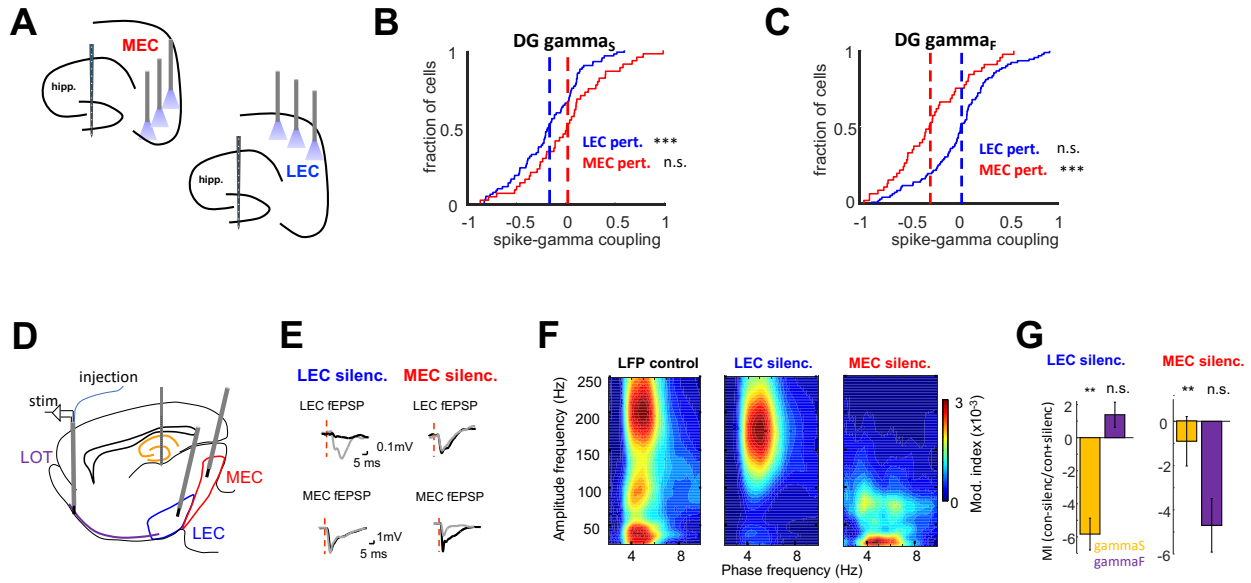


**Figure S9: Characterization of MEC and LEC gamma oscillations in the DG-CA3 regions**

**A)** Schema of the experiment. **B)** LEC perturbation reduced the strength of spike-gammas phase coupling for combined CA3/DG cells compared to baseline ( $P = 6.8e-6$ ,  $n = 98$  cells from 6 rats, signed-rank test). MEC perturbation did not affect spike-gammas phase coupling ( $P = 0.76$ ,  $n = 85$  cells from 6 rats). **C)** MEC perturbation reduced the strength of spike-gamma<sub>F</sub> phase coupling for combined CA3/DG cells compared to baseline ( $P = 1.6e-6$ ). LEC perturbation did not affect spike-gamma<sub>F</sub> phase coupling ( $P = 0.25$ ). **D-G)** Acute experiment under urethane anesthesia illustrates the EC origin of DG ICs. **D)** Experimental design. Three bipolar stimulation electrodes coupled to drug-injection polyamide tubes were placed in the lateral olfactory tract (LOT, purple), lateral (LEC, blue) and medial (MEC, red) entorhinal cortices, and a single-shank silicon probe in the hippocampus of urethane anaesthetized rats ( $n = 4$ ). **E)** Local lidocaine injections were used to transiently silence LEC or MEC ( $n = 4$  rats). After local lidocaine injection in LEC, LEC evoked potentials in DG were severely reduced (black lines) compared to control (grey lines), while MEC evoked potentials were largely unaffected. Conversely, lidocaine injection in MEC had complementary effects. **F)** Three different theta-modulated gamma oscillations of largely similar frequencies than those described in drug-free animals were observed in the granule layer (gammas, gamma<sub>M</sub> and gamma<sub>F</sub>; left comodulogram), despite slower theta frequency (~4Hz) during light urethane anesthesia. Following lidocaine injection in LEC, DG gamma<sub>S</sub> oscillations were reduced (middle comodulogram). Conversely, after MEC silencing, DG gamma<sub>F</sub> oscillations were impaired (right plot). **G)** Group data for modulation index (MI) ratios for the DG gammas and gamma<sub>F</sub> sub-bands (\*\*  $P < 0.01$ , sign-rank test,  $n= 4$  rats).

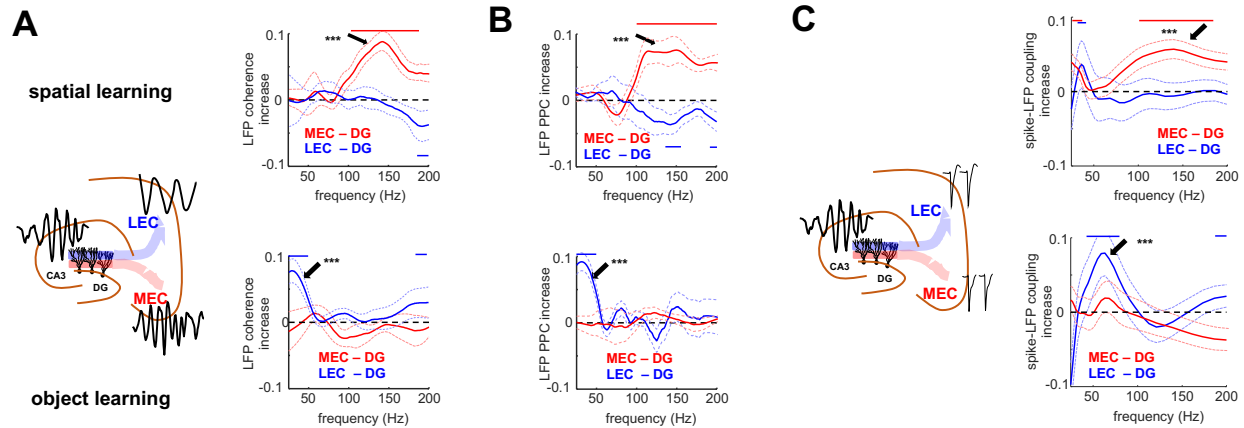


**Figure S10: Gamma synchrony between MEC, LEC and DG during learning**

**A-B)** Gamma LFP-LFP synchrony was measured using two additional metrics, in addition to the one shown in main Figure 4: LFP coherence (**A**) and pairwise-phase consistency (**B**). Top and bottom plots show learning-induced changes between baseline and learning sessions for MEC-DG and LEC-DG LFP-LFP gamma synchrony in the spatial and object learning tasks, respectively. Mean  $\pm$  SEM (learning-baseline)/(learning+baseline) ( $n= 12/12$  sessions in 4/4 rats for MEC/LEC, respectively). LFP traces were taken from the DG molecular layer and EC layer 2. Red and blue horizontal lines indicate frequencies with a significant effect ( $p < 0.05$ , Bonferroni correction for multiple comparisons). Asterisks denote significance level for synchrony changes respect to baseline averaged in the band of interest (\*\*\*( $P < 0.001$ , signed-rank test)). **C)** Spike-gamma LFP coupling (mean resultant length). Top and bottom plots show spike-LFP-spike coupling between spikes of layer II MEC excitatory neurons (red) and DG gamma LFP and spike of layer II LEC excitatory neurons and DG gamma LFP (blue) during spatial (top) or object (bottom) learning, respectively ( $n = 192/95$  MEC cells in the spatial and object tasks and  $n = 72/128$  LEC cells, from 4 rats in each case). Note that the three measures showed similar results. Compare with data in main Figure 4.

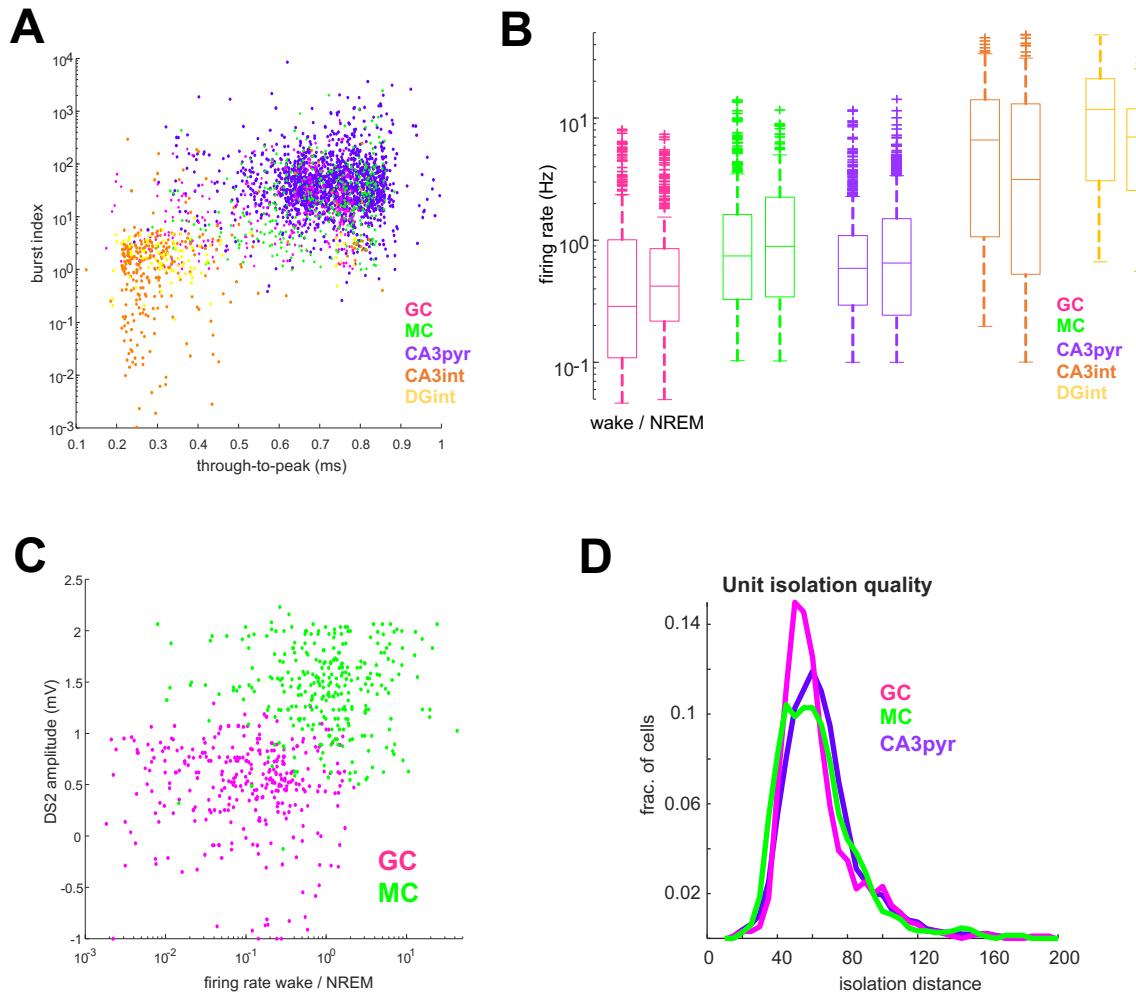


**Figure S11: CA3/DG cell type classification**

**A)** Scatter plot for all CA3-DG single units (1554 CA3 pyramidal cells, 377 granular cells -GC-, 323 mossy cells -MC-, 304 CA3 interneurons and 197 DG interneurons, from 95 sessions in 20 rats) showing the separation of putative excitatory and inhibitory units based of waveform width (through-to peak duration) and proportion of burst firing. **B)** Mean firing rates during non-REM sleep and wake states for each cell class. **C)** DG excitatory units displayed as a function of their wake/ non-REM firing rate ratio and amplitude of dentate spikes 2 (DS2) in the electrode were each cell largest amplitude waveform was recorded. **D)** Cluster isolation distance for GC, MC and CA3pyr.

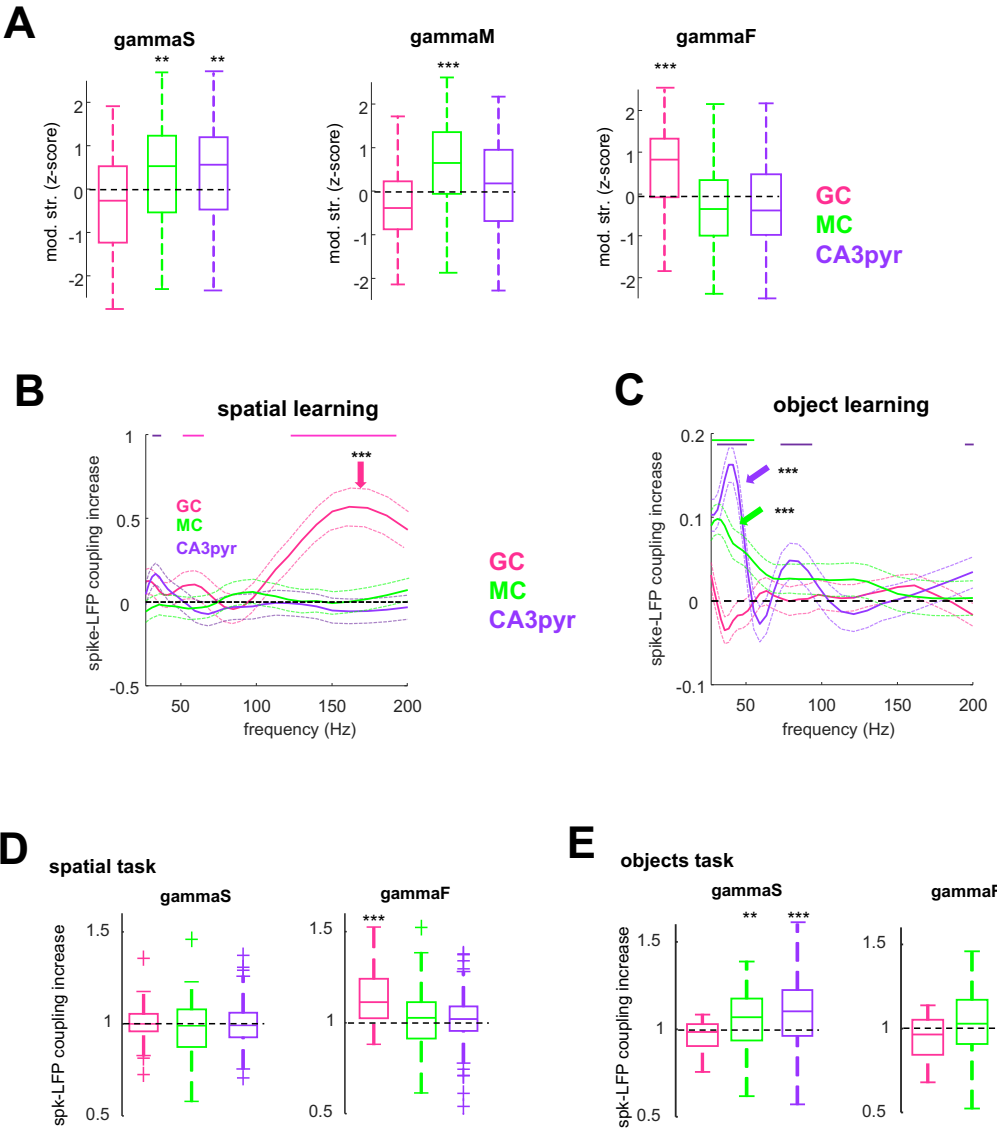


**Figure S12: Spike-gamma LFP coupling of CA3/DG neuron sub-populations**

**A)** GC, MC and CA3 pyramidal neuron mean spike – gamma LFP phase modulation strength for the three DG gamma sub-bands. \*\*/\*\*\*  $P < 0.01/0.001$ , sign-rank test. **B)** During spatial learning spike-gamma<sub>F</sub> coupling (mean resultant length) selectively increased for GC (arrow) but not for MC and CA3 pyramidal cells ( $P = 6.2e-11$  n = 201; MC  $P = 0.17$ , n = 145; CA3pyr  $P = 0.43$ , n = 704). Y axis, difference between learning session and pre-learning exploration session. Horizontal color lines indicate frequencies with a significant effect for the respective cell types ( $p < 0.05$ , Bonferroni correction for multiple comparisons). **C)** Same as **B**) but during object learning. Spike-gammas coupling increased for MCs and CA3pyr (arrows) but not for GC (GC  $P = 0.14$  n= 130, MC  $P= 2.0e-19$  n= 111, CA3pyr  $P= 1.8e-32$  n= 548). **D)** GC, MC and CA3pyr spike – gamma LFP coupling selectively increased during spatial learning trials compared to baseline period for MEC gamma<sub>F</sub> and LEC gammas. Note largely similar patterns of all measures for MC and CA3 (mainly CA3c) pyramidal cells and different patterns for GC. \*\*\*  $P < 0.001$ , sign-rank test. **E)** Same as in E but for the object learning task. \*\*/\*\*\*  $P < 0.01/0.001$ .

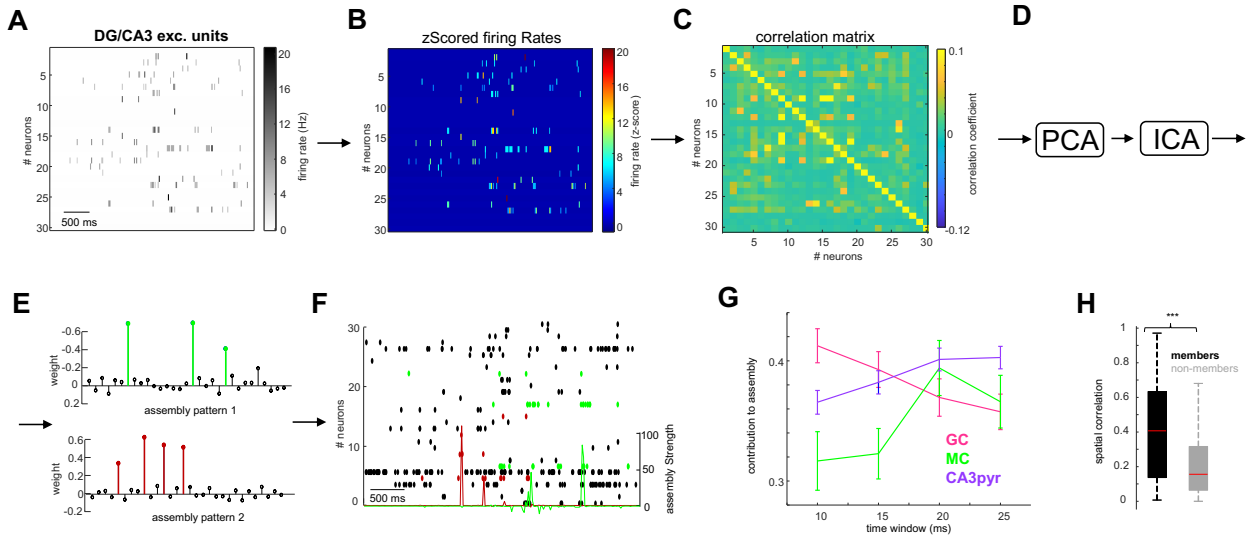


**Figure S13: Method of identification and tracking of hippocampal cell assemblies**

**A-D)** Schematic of the procedure to identify cell assembly activation patterns. **A)** Spike raster fragment of 30 simultaneously recorded DG/CA3 excitatory units. **B)** Each neuron spike train was binned in 20 ms windows and normalized (z-scored). **C)** Correlation matrix of the binned spike trains during the task. **D)** Principal Component Analysis (PCA) was applied to the correlation matrix C to find the number of statistically significant assembly patterns. Next, ICA was applied to the significant PCA subspace of the data to find the weight of the assembly patterns across all neurons (see Methods). **E)** Two example assembly patterns. The height of each bar represents the magnitude of contribution of that neuron to the assembly. Assembly members (colored bars) were termed as those neurons whose contribution weight exceeded 2 standard deviations above the mean of that assembly. **F)** Example unit firing raster and the temporal activation of the two assembly patterns in **E**. Assembly temporal activations were obtained by multiplying the convolved spike trains with the assembly weight vector. **G)** Average contribution to assembly reactivation of each cell type. To evaluate the preferred temporal scale of assembly activation, spiking activity was binned using different time windows (10-25 ms). To increase statistical power, assemblies in the spatial and object tasks were pooled. **H)** Spatial correlation of the firing maps during spatial learning trials of assembly members ( $n= 910$  pairs) was significantly higher than that of non-member cells ( $n = 78404$  pairs,  $P = 5.8\text{e-}14$ , rank-sum test)

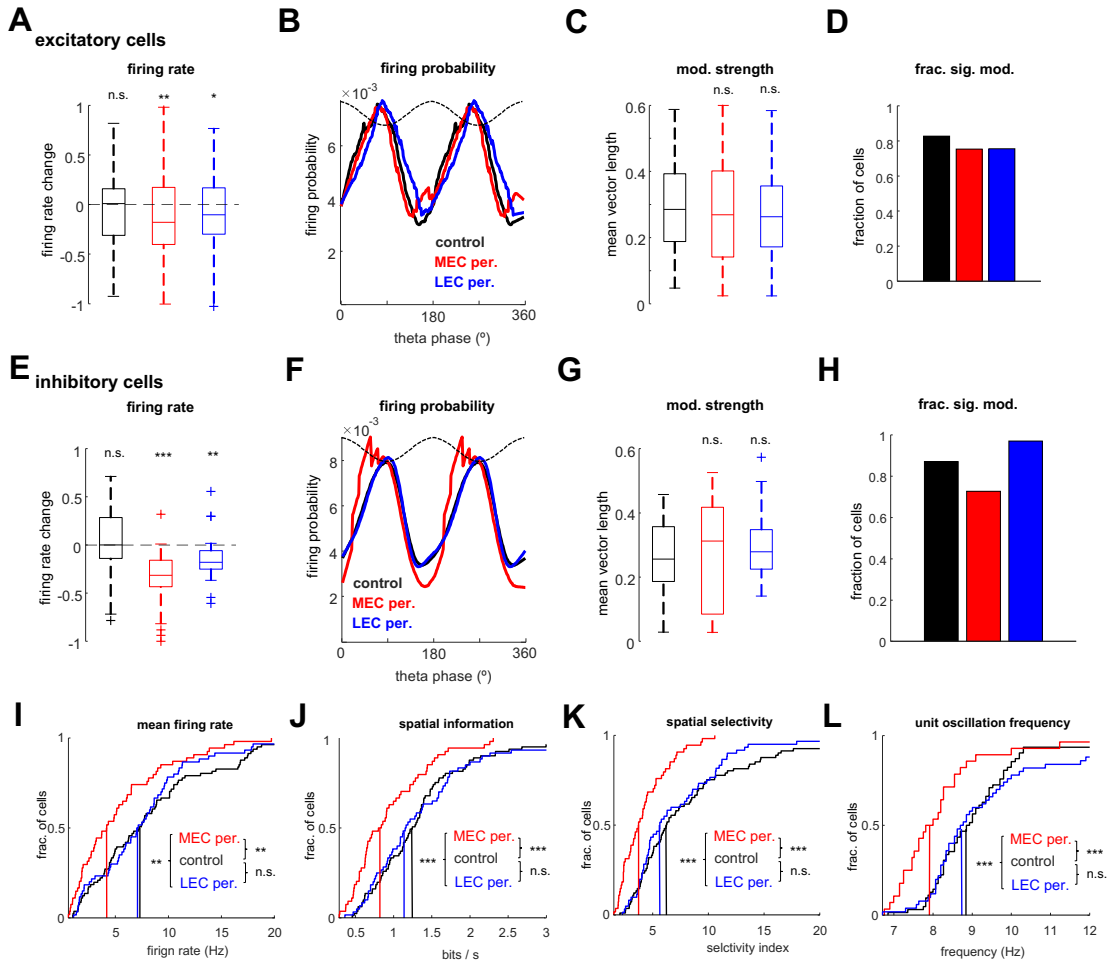


**Figure S14: Effect of entorhinal optogenetic perturbation on the firing of CA3-DG cells**

**A)** Firing rate changes [(baseline-perturb.)/(baseline+perturb.)] for combined CA3-DG excitatory cells during control, MEC and LEC perturbation sessions ( $n = 127/85/98$  neurons, respectively, from 10 rats).  $*/** P < 0.05/ 0.01$ , sign-rank test. **B)** Theta phase firing probability distribution, mean vector length (**C**) and (**D**) fraction of significantly modulated units ( $P > 0.05$ , Rayleigh test) for excitatory cells were not different during control, MEC and LEC perturbation sessions (n.s.,  $P > 0.05$ , rank-sum test). **E-H)** Same layout as in A-D but for putative CA3-DG inhibitory cells ( $n = 31/22/34$  interneurons during control, MEC and LEC perturbations, respectively, from 10 rats).  $**/*** P < 0.01/ 0.001$ , sign-rank test. **I-L)** Additional spatial coding metrics for CA3-DG place cells during spatial learning trials ( $n = 81/54/60$  place cells from control, MEC and LEC perturbation sessions respectively). Vertical lines indicate medians of the distributions: (**I**) mean firing rate within the place field ( $P = 1.4e-3/ 0.73$ , rank-sum test, for MEC and LEC perturbation sessions compared to control sessions); (**J**) spatial information in bits per s ( $P = 1e-4/ 0.86$ ; note that in Fig. 7E spatial information is expressed instead in bits per spike); (**K**) spatial selectivity ( $p = 1.4e-7/ 0.41$ ); (**L**) Theta band oscillation frequency of all principal neurons within their place fields ( $P = 7.5e-5/ 0.96$ ). Note the decrease of theta-band oscillation frequency of spikes during LFP perturbation, despite no change of LFP theta frequency (Fig. S1G) by MEC optogenetic stimulation. This finding illustrates that it is the sub-theta timing of DG neuron spikes (Mizuseki et al., 2009) that was affected by the MEC perturbation.